Computers and Chemical Engineering 123 (2019) 246–256

Contents lists available at ScienceDirect

Computers and Chemical Engineering

journal homepage: www.elsevier.com/locate/compchemeng

Coupling of the population balance equation into a two-phase model for the simulation of combined cooling and antisolvent crystallization using OpenFOAM

Lauren F.I. Farias[a,b], Jeferson A. de Souza[a], Richard D. Braatz[c], Cezar A. da Rosa[a,*]

[a] Federal University of Rio Grande, Av. Itália km 8 Bairro Carreiros, 96203-900, Rio Grande, RS, Brazil
[b] Federal University of Pelotas, St. Benjamin Constan Bairro Centro, 96010-020, Pelotas, RS, Brazil
[c] Massachusetts Institute of Technology, 77 Massachusetts Avenue, Cambridge, MA 02139, United States

ARTICLE INFO

Article history:
Received 16 April 2018
Revised 27 December 2018
Accepted 6 January 2019
Available online 10 January 2019

Keywords:
Two-phase model
Population balance models
Pharmaceutical manufacturing
Computational fluid dynamics
Pharmaceutical crystallization

ABSTRACT

This article proposes a two-phase Eulerian-Eulerian model coupled with granular kinetic theory, semi-discrete population balance equations, energy balance, and scalar transport equations for the simulation of the full crystal size distribution and the effects of particle settling in continuous-flow crystallizers. The model capabilities are demonstrated by application of an OpenFOAM® implementation to the combined cooling/antisolvent crystallization of Lovastatin in a coaxial mixer. The simulations show that (1) the spatial fields for the antisolvent mass fraction and crystal nucleation and growth rates can be highly asymmetric for small continuous-flow crystallizers, (2) continuous-flow crystallizers of small dimension can generate bimodal crystal size distributions, and (3) a relatively small change in the inlet feed velocity can change the crystal size distribution from being unimodal to bimodal. These results demonstrate the potential of the proposed model for gaining insights into continuous-flow crystallization that can be useful for the design of equipment or operations.

1. Introduction

Crystallization is one of the most important separation and purification techniques in the manufacturing of high-value products such as fine chemicals and pharmaceuticals. In this multiphase process, simultaneous heat and mass transfer occur and the crystal size distribution (CSD) and other states vary with space and time (Mullin, 2001).

Among various methods of crystallization used by the industry, especially by the pharmaceutical industry, antisolvent addition is commonly used for inducing crystallization for thermally sensitive pharmaceuticals by limiting large temperature variations (Wey and Karpinski, 2002). Also applied in industry are combined cooling and antisolvent crystallization (e.g., Nagy et al., 2008; Jiang et al., 2015; Schall et al., 2018), in which both cooling and antisolvent are employed, primarily to generate higher yields than can be achieved separately.

Several crystallizer designs have been investigated, including batch and semi-batch stirred tanks and mixed-suspension mixed-product removal (MSMPR), dual-impinging jet, coaxial, and radial mixer-based continuous-flow crystallizers (Jiang et al., 2015; Li et al., 2015; Pirkle et al., 2015; Yu et al., 2016; Cheng et al., 2017; da Rosa and Braatz, 2018). Continuous operation has some advantages that include improved product consistency, yield, and capacity, and lower facility cost and space requirements (e.g., Wang et al., 2017). An important consideration in the design of continuous-flow crystallizers is to suppress encrustation (e.g., Powell et al., 2015), which is also commonly referred to as "fouling." Encrustation in continuous-flow crystallizers and heat transfer device operation has been modeled (e.g., Brahim et al., 2003; Koswara and Nagy, 2017; Majumder and Nagy, 2015; Pääkkönen et al., 2016). Encrustation depends on spatially localized values for the states, and better models are needed of the fluid flow and operating conditions during crystallization to be able to accurately predict encrustation, at which point the equipment and operations can be designed to suppress encrustation.

Different approaches can be employed to model fluid-particle flows with particle size distribution and the inclusion of gravity effects, e.g., Eulerian-Lagrangian, Eulerian-Eulerian. The Eulerian-Eulerian, also called two-fluid-model, combined with the population balance equation has been successfully applied to simulate the evolution and growth of the particle size in gas–solid rotating fluidized bed olefin polymerization (Ahmadzadeh et al., 2008) and to calculate the variation of the particle properties during a CO_2

* Corresponding author.
E-mail address: cezar.rosa@furg.br (C.A. da Rosa).

https://doi.org/10.1016/j.compchemeng.2019.01.009
0098-1354/

Nomenclature

B	Nucleation rate
c	Concentration of solute
c^*	Solubility or saturation concentration
D_t	Turbulent diffusivity
e_{ss}	Restitution coefficient
f	Number density function
f_r	Derivative of number density function
f_w	Mass basis density function
$\vec{g}$	Gravitational acceleration
G	Growth rate
h	Enthalpy per unit mass
k	Turbulent kinetic energy
k_v	Volume shape factor
$\dot{m}$	Mass transfer rate between phases
p	Pressure in momentum conservation equation
p_s	Crystals phase pressure
r	Crystal size
r_0	Nuclei size
$\mathrm{Re_s}$	Particle Reynolds number
S	Relative supersaturation = c/c*
$S_{w,j}$	Source term due to crystallization
S_ϕ	Source term in components transport equations
t	Time
T	Temperature
$\vec{v}$	Velocity vector

Symbols

Δc	supersaturation = c − c*
Δr	Discretized bin size for crystal size
Γ_k	Effective mass diffusion coefficient
Θ	Granular temperature
α	Volume fraction
β_{ls}	Momentum transfer coefficient
ε	Turbulent kinetic energy dissipation rate
ϕ	Energy exchange between phases in the granular temperature equation
	Mass fraction in the multicomponent mixture model
γ_s	Collisional dissipation of energy
λ	Solids bulk viscosity in granular kinetic model
μ	Viscosity
μ_{eff}	effective shear viscosity
μ_t	Turbulent viscosity
ρ	Density
$\bar{\bar{\tau}}$	Stress tensor

Subscripts

c	Crystal
f	Face interpolation
j	Discretized bin for crystal size in population balance equation
k	Component index in multicomponent model
l	Liquid phase
s	Crystals phase
w	Mass basis in population balance equation

capture using MgO-based sorbent (Abbasi et al., 2015). However, there is a lack of information regarding the application of such models to simulate crystallization processes and to predict "fouling" formation in continuous-flow crystallizers.

This article couples the population balance equation with a two-fluid model, based on the Eulerian-Eulerian formulation and the granular kinetic theory (Gidaspow, 1994), to model and simulate combined cooling and antisolvent crystallization in continuous-flow crystallizers and to predict likely locations for crystal deposition. For that purpose, a set of semi-discrete population balance equations, using a high resolution finite-volume method, was coupled to a two-phase Eulerian-Eulerian using the open-source CFD package OpenFOAM®. The methanol-water cooling and antisolvent crystallization of lovastatin, using kinetics reported in the literature (Mahajam and Kirwan, 1994), and the continuous-flow coaxial crystallizer geometry studied by Pirkle et al. (2015), was chosen as the model system in the simulations. The case study, results and discussion, and conclusions are presented after the model equations, model implementation, and numerical methods.

2. Model equations

This article employs a two-phase model, based on the Eulerian-Eulerian approach, and the granular kinetic theory to account for the flow properties of the particle phase. The evolution of the crystal size distribution (CSD) is modeled by a set of semi-discrete population balance equations, derived using a high resolution finite-volume discretization method, that was coupled to the two-phase model. The fluid phase is treated as an ideal multicomponent mixture, and scalar transport equations are used to account for the mass conservation of each component. Also, energy balance equations are employed to model the intra- and interphase heat transfer.

2.1. Mass and momentum conservation

The continuity equations for the two liquid (l) and crystal (s) phases are

$$\frac{\partial}{\partial t}(\alpha_l\rho_l) + \nabla\cdot(\alpha_l\rho_l\vec{v}_l) = -(\dot{m}_{ls} - \dot{m}_{sl}) \tag{1}$$

$$\frac{\partial}{\partial t}(\alpha_s\rho_s) + \nabla\cdot(\alpha_s\rho_s\vec{v}_s) = (\dot{m}_{ls} - \dot{m}_{sl}) \tag{2}$$

where α is the volume fraction and $(\dot{m}_{ls} - \dot{m}_{sl})$ is the net mass transfer rate between the phases due to crystallization and/or crystals dissolution. The conservation of momentum equations for the two phases are

$$\frac{\partial}{\partial t}(\alpha_l\rho_l\vec{v}_l) + \nabla\cdot(\alpha_l\rho_l\vec{v}_l\vec{v}_l) = -\alpha_l\nabla p + \nabla\cdot\bar{\bar{\tau}}_l + \alpha_l\rho_l\vec{g} - \beta_{ls}(\vec{v}_l - \vec{v}_s) + \dot{m}_{sl}\vec{v}_s - \dot{m}_{ls}\vec{v}_l \tag{3}$$

$$\frac{\partial}{\partial t}(\alpha_s\rho_s\vec{v}_s) + \nabla\cdot(\alpha_s\rho_s\vec{v}_s\vec{v}_s) = -\alpha_s\nabla p - \nabla p_s + \nabla\cdot\bar{\bar{\tau}}_s + \alpha_s\rho_s\vec{g} - \beta_{ls}(\vec{v}_s - \vec{v}_l) - \dot{m}_{sl}\vec{v}_s + \dot{m}_{ls}\vec{v}_l \tag{4}$$

where $\beta_{ls}(\vec{v}_l - \vec{v}_s)$ is the interphase momentum transfer due to the drag force, and $\dot{m}_{sl}\vec{v}_{sl}$ and $\dot{m}_{ls}\vec{v}_{ls}$ are extra terms to account for the interphase momentum transfer due to mass transfer between phases. p_s in (4) is the solids pressure or the normal stress of the granular phase which consists of consists of the kinetic pressure due to the motion of the particles and a collisional pressure due to inelastic collision of particles (Lun et al., 1984).

The liquid phase is assumed to be a Newtonian fluid, and the Boussinesq hypothesis for the turbulent stress-strain,

$$\bar{\bar{\tau}}_l = \alpha_l\mu_{\mathrm{eff}}\left[\nabla\vec{v}_l + (\nabla\vec{v}_l)^{\mathrm{T}} - \frac{2}{3}(\nabla\cdot\vec{v}_l)\bar{\bar{I}}\right] - \frac{2}{3}\alpha_l\rho_l k_l\bar{\bar{I}}, \tag{5}$$

is used, where $\mu_{\mathrm{eff}} = \mu_l + \mu_l^t$ is the effective shear viscosity of the liquid phase, k_l is the turbulent kinetic energy, and $\bar{\bar{I}}$ is the identity

tensor. Turbulence effects in the fluid phase were modeled by the standard k-ε model.

In a similar way, the shear stress of the particle phase is expressed as

$$\bar{\bar{\tau}}_s = \alpha_s \mu_s \left[\nabla \vec{v}_s + (\nabla \vec{v}_s)^{\mathrm{T}}\right] + \alpha_s \left(\lambda_s - \frac{2}{3}\mu_s\right)(\nabla \cdot \vec{v}_s)\bar{\bar{I}} \tag{6}$$

where μ_s and λ_s are the particle shear viscosity and bulk viscosity, respectively, which are calculated via granular kinetic theory (Gidaspow, 1994).

2.2. Particle drag model

The studied crystallizer conditions are within the dilute particulate flow regime, for which the momentum transfer coefficient β_{ls} given by (Wen and Yu, 1966)

$$\beta_{ls} = \frac{3}{4} C_D \frac{\alpha_l \alpha_s \rho_l |\vec{v}_s - \vec{v}_l|}{d_s} \alpha_l^{-2.65} \tag{7}$$

where

$$C_D = \frac{24}{\alpha_l \mathrm{Re}_s}\left[1 + 0.15(\alpha_l \mathrm{Re}_s)^{0.687}\right] \tag{8}$$

and

$$\mathrm{Re}_s = \frac{\rho_l |\vec{v}_s - \vec{v}_l| d_s}{\mu_l} \tag{9}$$

is the particle Reynolds number.

2.3. Granular kinetic theory equations

The momentum equation requires a description of the solid-phase shear stress and pressure, for which the granular kinetic theory of Gidaspow (1994) is adopted. Analogous to the thermodynamic temperature for gases, the granular temperature ($\Theta_s\Theta_s$) is introduced as a measure of the particle velocity fluctuations,

$$\Theta_s = \frac{1}{3}\left(v_s'\right)^2, \tag{10}$$

where $v_s' v_s'$ is the particle fluctuating velocity. That is, the granular temperature for the solid phase is proportional to the kinetic energy of the random motion of the particles. The conservation of granular temperature equation is

$$\frac{3}{2}\left[\frac{\partial}{\partial t}(\alpha_s \rho_s \Theta_s) + \nabla \cdot (\alpha_s \rho_s \vec{v}_s \Theta_s)\right] = \left(-p_s \bar{\bar{I}} + \bar{\bar{\tau}}_s\right) : \nabla \vec{v}_s + \nabla \cdot (k_{\Theta s} \nabla \Theta_s) - \gamma_s + \phi_{ls} \tag{11}$$

where $(-p_s \bar{\bar{I}} + \bar{\bar{\tau}}_s) : \nabla v_s$ is the generation of energy by the solid stress tensor, $k_{\Theta s}\nabla\Theta_s$ is the diffusion of energy, $\gamma_s \gamma_{\Theta_s}$ is the collisional dissipation of energy, and ϕ_{ls} is the energy exchange between the fluid phase and the solid phase. The diffusion coefficient for granular energy (k_{Θ_s}) and the energy exchange between phases (ϕ_{ls}) were calculated as in Gidaspow et al. (1992). The collisional dissipation of energy was modeled according to Lun et al. (1984).

The solids stress tensor contains the shear and bulk viscosities arising from particle momentum exchange due to translation and collision. The collisional and kinetic parts are added to give the solids shear viscosity. The frictional viscosity term is not included because all of the conditions studied here fall within the dilute flow regime.

The collisional and kinetic parts of the shear viscosity are given by (Gidaspow et al., 1992)

$$\mu_{s,col} = \frac{4}{5}\alpha_s^2 \rho_s d_s g_{0,ss}(1 + e_{ss})\left(\frac{\Theta_s}{\pi}\right)^{1/2} \tag{12}$$

$$\mu_{s,kin} = \frac{10\rho_s d_s \sqrt{\Theta_s \pi}}{96(1 + e_{ss}) g_{0,ss}}\left[1 + \frac{4}{5}\alpha_s g_{0,ss}(1 + e_{ss})\right]^2 \tag{13}$$

The solids bulk viscosity, which accounts for the resistance of the granular particles to compression and expansion, is given by (Lun et al., 1984)

$$\lambda_s = \frac{4}{3}\alpha_s \rho_s d_s g_{0,ss}(1 + e_{ss})\left(\frac{\Theta_s}{\pi}\right)^{1/2} \tag{14}$$

The solids pressure was calculated from (Lun et al., 1984)

$$p_s = \alpha_s \rho_s \Theta_s + 2\rho_s \alpha_s^2 g_{0,ss} \Theta_s (1 + e_{ss}) \tag{15}$$

where e_{ss} is the restitution coefficient and $g_{0,\,ss}$ is the radial distribution function (Ogawa et al., 1980).

2.4. Energy conservation

The intra- and interphase heat transfer was modeled by applying an energy conservation equation to the fluid phase

$$\frac{\partial}{\partial t}(\alpha_l \rho_l h_l) + \nabla \cdot (\alpha_l \rho_l \vec{v}_l h_l) = -\nabla \cdot \vec{q}_l - \dot{Q}_{ls} + \dot{m}_{sl} h_{sl} - \dot{m}_{ls} h_{ls} \tag{16}$$

and to the crystals phase

$$\frac{\partial}{\partial t}(\alpha_s \rho_s h_s) + \nabla \cdot (\alpha_s \rho_s \vec{v}_s h_s) = -\nabla \cdot \vec{q}_s + \dot{Q}_{fs} - \dot{m}_{sf} h_{sf} + \dot{m}_{fs} h_{fs} \tag{17}$$

These equations include the energy transfer due to crystallization ($\dot{m}_{ls}h_{ls}$) and/or dissolution ($\dot{m}_{sl}h_{sl}$) and the convective interphase heat transfer ($\dot{Q}_{ls}$). The convective interphase heat transfer was modeled by the Newton's law of cooling analogous equation, and the convective heat transfer coefficient was calculated based on the Nusselt number correlation of Ranz and Marshall (1952). $\vec{q}$ in (16) and (17) is the conductive heat flux which is modelled by the Fourier's law. In this work, the conductive heat transfer in the crystals phase was neglected by setting the thermal conductivity to zero.

2.5. Fluid-phase multicomponent model

The fluid phase was considered to be a multicomponent ideal mixture, composed by the solvent (methanol), solute (lovastatin), and antisolvent (water). Since the concentration of these components vary with time and space, due to the boundary conditions and crystallization, mass transport equations are applied to model each component (k), as described by

$$\frac{\partial}{\partial t}(\alpha_l \rho_l \phi_k) + \nabla \cdot (\alpha_l \rho_l \vec{v}_l \phi_k) = \nabla \cdot (\alpha_l \Gamma_k \nabla \phi_k) + S_{\phi_k} \tag{18}$$

where ϕ_k is the mass fraction of the k component and S_{ϕ_k} is the source term due to mass generation and/or consumption of the k component.

2.6. Population balance equation

The crystallization is described by the spatially inhomogeneous population balance equation (PBE),

$$\frac{\partial f}{\partial t} + \sum_i \frac{\partial [G_i(r_i, c, T) f]}{\partial r_i} + \nabla \cdot (\vec{v} f - D_t \nabla f) = B(f, c, T) \prod_i \delta(r_i - r_{i0}) + h(f, c, T), \tag{19}$$

where f is the particle number density function, which is a function of external coordinates (X, Y, and Z in the Cartesian 3D case),

the internal coordinates r_i (the size dimensions of the crystals), and the time t (Randolph and Larson, 1988). The growth rates $G_i = dr_i/dt$ and the nucleation rate B are functions of the vector of solution concentrations c and the temperature T, δ is the Dirac delta function, and h describes the creation and destruction of crystals due to aggregation, agglomeration, and breakage. For size-dependent growth, the growth rates G_i also vary with the internal coordinates r_i.

To couple with the CFD solver, the PBE (19) is rewritten on a mass basis,

$$f_{w,j} = \rho_c k_v \int_{r_{j-1/2}}^{r_{j+1/2}} r^3 f_j dr = \frac{\rho_c k_v f_j}{4}\left[\left(r_{j+1/2}\right)^4 - \left(r_{j-1/2}\right)^4\right], \quad (20)$$

where $f_{w,j}$ is the cell-averaged crystal mass with units of kg/m^3. The PBE is discretized along the growth axis using a high-resolution finite volume method (Woo et al., 2006). Differently from past work which used single-phase CFD (Woo et al., 2006; 2009; Pirkle et al., 2015), this article couples the set of semi-discrete PBE to a two-phase CFD model. Since the PBE is applied only to the crystals phase in this formulation, the PBE must be converted to the same volumetric basis. Therefore the volume fraction concept is introduced in the semi-discrete set of equations, as

$$\frac{\partial}{\partial t}\left(\alpha_s f_{w,j}\right) + \nabla \cdot \left(\alpha_s \vec{v}_s f_{w,j}\right) = \nabla \cdot \left(\alpha_s D_t \nabla f_{w,j}\right) + \alpha_s S_{w,j} \quad (21)$$

where $S_{w,j}$ is the source term due to crystal nucleation and growth, which is calculated from

$$S_{w,j} = \frac{\rho_c k_v}{4\Delta r}\left[\left(r_{j+1/2}\right)^4 - \left(r_{j-1/2}\right)^4\right]\left\{-G_{j+\frac{1}{2}}\left[f_j + \frac{\Delta r}{2}(f_r)_j\right] + G_{j-\frac{1}{2}}\left[f_{j-1} + \frac{\Delta r}{2}(f_r)_{j-1}\right] + B\delta_{j0}\right\} \quad \text{for } \Delta c \geq 0 \quad (22)$$

$$S_{w,j} = \frac{\rho_c k_v}{4\Delta r}\left[\left(r_{j+1/2}\right)^4 - \left(r_{j-1/2}\right)^4\right]\left\{-G_{j+\frac{1}{2}}\left[f_{j+1} - \frac{\Delta r}{2}(f_r)_{j+1}\right] + G_{j-\frac{1}{2}}\left[f_j - \frac{\Delta r}{2}(f_r)_j\right]\right\} \text{otherwise} \quad (23)$$

where $\Delta r = r_{j+1/2} - r_{j-1/2}$, ρ_c is the crystal density, k_v is the crystal volume shape factor, $(f_r)_j$ is the derivative approximated by the minmod-limiter (Kurganov and Tadmor, 2000), Δc is the supersaturation, and δ_{ji} is the Kronecker delta (which is defined to be equal to one when $i = j$ and zero otherwise).

3. Model implementation and numerical solution

The model equations were implemented in OpenFOAM® 4.0 via object-oriented C++ programing language as in Passalacqua and Fox (2011) and Liu and Hinrichsen (2014). A set of dictionaries was used to input the transport and PBE properties. The semi-discretized PBE equations, resulting from PBE growth axis discretization, were implemented in OpenFOAM® code using the PtrList<T> C++ template, which constructs an array of classes or templates of type T. In order to calculate the source terms of the PBEs, the minmod-limiter and the functions for calculating supersaturation, crystal growth and nucleation were implemented in a separated C++ object, which makes it easier to customize the code for different crystallization kinetics.

3.1. Discretization of the model equations

The fully conservative form of the momentum equations was adopted in this work. In order to avoid obtaining a singular system of linear algebraic equations, the momentum equation was not solved in the computational cells where the phase volume fraction is lower than a certain minimum value (Passalacqua and Fox, 2011).

As mentioned before, the liquid phase is considered to be a multicomponent ideal mixture, with extra scalar transport equations to account for the mass conservation of mixture components. As such, the density of the mixture is a function of both spatial coordinates and time (while the density of the crystals phase is constant). The semi-discrete form of (3) and (4) with constant density are

$$A_l \vec{v}_l = H_l - \alpha_l \nabla P + \alpha_l \rho_l \vec{g} - \beta_{ls}(\vec{v}_l - \vec{v}_s) + \dot{m}_{sl}\vec{v}_s - \dot{m}_{ls}\vec{v}_l \quad (24)$$

$$A_s \vec{v}_s = H_s - \frac{\alpha_S}{\rho_S}\nabla P - \frac{1}{\rho_S}\nabla P_s + \alpha_s \vec{g} - \frac{\beta_{fs}}{\rho_S}(\vec{v}_s - \vec{v}_l) - \frac{\dot{m}_{sl}}{\rho_s}\vec{v}_s + \frac{\dot{m}_{ls}}{\rho_s}\vec{v}_l \quad (25)$$

where A represents the diagonal coefficients of the velocity matrix and H consists of the off-diagonal and source terms apart from the pressure gradient (e.g., as in Eq. 3.137 of Jasak, 1996).

Grouping the terms containing the unknown velocities in these equations results in equations for the intermediate phase velocities,

$$\vec{v}_l = \lambda_l(H_l - \alpha_l \nabla P + \alpha_l \rho_l \vec{g}) + \lambda_l(\beta_{ls} + \dot{m}_{sl})\vec{v}_s \quad (26)$$

$$\vec{v}_s = \lambda_s\left(H_s - \frac{\alpha_s}{\rho_s}\nabla P - \frac{1}{\rho_s}\nabla P_s + \alpha_s \vec{g}\right) + \lambda_s\left(\frac{\beta_{ls} + \dot{m}_{ls}}{\rho_s}\right)\vec{v}_l \quad (27)$$

where λ_l and λ_s are given by

$$\lambda_l = \frac{1}{A_l + \dot{m}_{ls} + \beta_{ls}} \quad (28)$$

$$\lambda_s = \frac{1}{A_s + \frac{\beta_{ls} + \dot{m}_{sl}}{\rho_s}} \quad (29)$$

Substituting (26) into (25) and (27) into (24) results in two decoupled expressions for the intermediate phase velocities,

$$\vec{v}_l = \frac{1}{A_l^*}\left\{\begin{array}{l} H_l + \lambda_s(\beta_{ls} + \dot{m}_{sl})H_s - (\alpha_l + \lambda_s \alpha_s \frac{\beta_{ls} + \dot{m}_{sl}}{\rho_s})\nabla P - \lambda_s \frac{\beta_{ls} + \dot{m}_{sl}}{\rho_s}\nabla P_s \\ + [\alpha_l \rho_l + \lambda_s \alpha_s(\beta_{ls} + \dot{m}_{sl})]\vec{g} \end{array}\right\} \quad (30)$$

$$\vec{v}_s = \frac{1}{A_s^*}\left[\begin{array}{l} H_s + \lambda_l \frac{\beta_{ls} + \dot{m}_{ls}}{\rho_s} H_l - \left(\frac{\alpha_s}{\rho_s} + \lambda_l \alpha_l \frac{\beta_{ls} + \dot{m}_{ls}}{\rho_s}\right)\nabla P - \frac{1}{\rho_s}\nabla P_s \\ + \left(\alpha_s + \lambda_l \alpha_l \rho_l \frac{\beta_{ls} + \dot{m}_{ls}}{\rho_s}\right)\vec{g} \end{array}\right] \quad (31)$$

where

$$A_l^* = A_l + \dot{m}_{ls} + \beta_{ls} - \lambda_S(\beta_{ls} + \dot{m}_{sl})\left(\frac{\beta_{ls} + \dot{m}_{ls}}{\rho_S}\right) \quad (32)$$

$$A_s^* = A_s + \left(\frac{\beta_{ls} + \dot{m}_{sl}}{\rho_s}\right) - \lambda_l(\beta_{ls} + \dot{m}_{sl})\left(\frac{\beta_{ls} + \dot{m}_{ls}}{\rho_s}\right) \quad (33)$$

3.2. Pressure equation and velocity fluxes correction

The pressure equation is obtained by imposing volumetric conservation,

$$\nabla \cdot \varphi = \nabla \cdot \left(\alpha_{l,f}\varphi_l + \alpha_{s,f}\varphi_s\right) = 0, \quad (34)$$

where φ_l and φ_s are the liquid and crystals phases velocity fluxes, respectively, which are calculated by interpolating (30) and (31) on cell faces and calculating the scalar product with the face normal

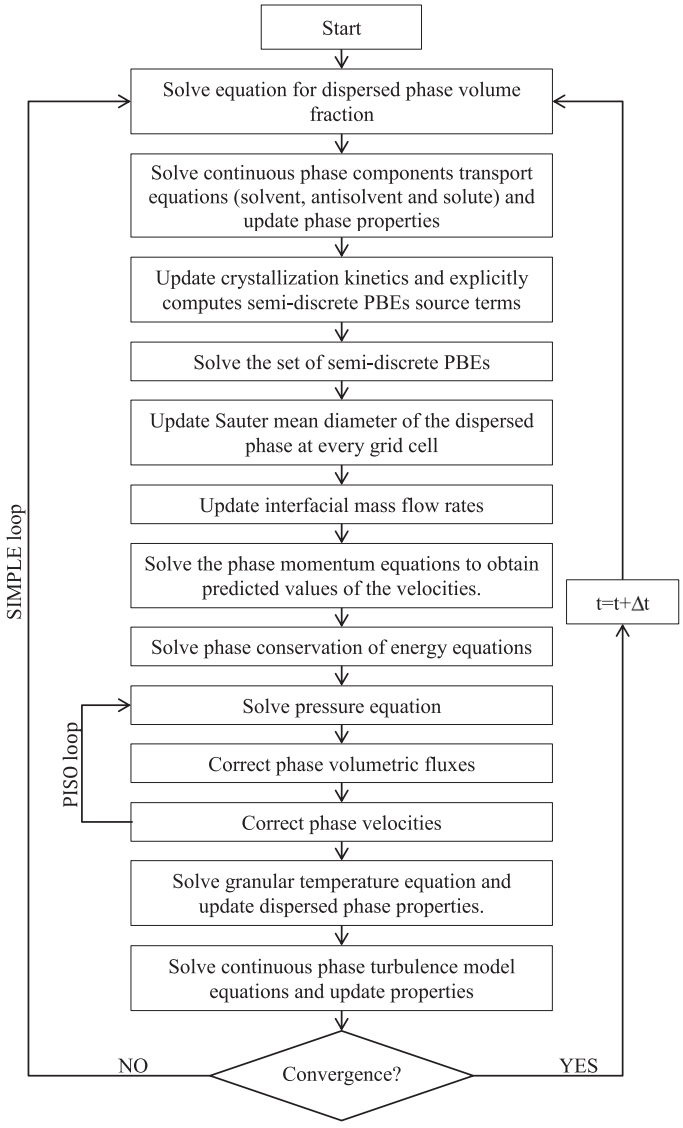

Fig. 1. Numerical solution procedure.

vector $\vec{S}$, as described in

$$\varphi_l = \frac{1}{A^*_{l,f}}[H_l + \lambda_S(\beta_{ls} + \dot{m}_{sl})H_s]_f \cdot \vec{S}$$

$$-\frac{1}{A^*_{l,f}}\left(\alpha_l + \lambda_s\alpha_s\frac{\beta_{ls} + \dot{m}_{sl}}{\rho_s}\right)_f \left|\vec{S}\right|\nabla^\perp P$$
$$-\frac{1}{A^*_{l,f}}\left(\lambda_s\frac{\beta_{ls} + \dot{m}_{sl}}{\rho_s}\right)_f \left|\vec{S}\right|\nabla^\perp P_s$$
$$+\frac{1}{A^*_{l,f}}[\ \alpha_l\rho_l + \lambda_s\alpha_s(\beta_{ls} + \dot{m}_{sl})]_f\vec{g}\cdot\vec{S} \quad (35)$$

$$\varphi_s = \frac{1}{A^*_{s,f}}\left(H_s + \lambda_l\frac{\beta_{ls} + \dot{m}_{ls}}{\rho_s}H_l\right)_f \cdot \vec{S}$$
$$-\frac{1}{A^*_{s,f}}\left(\frac{\alpha_s}{\rho_s} + \lambda_l\alpha_l\frac{\beta_{ls} + \dot{m}_{ls}}{\rho_s}\right)_f \left|\vec{S}\right|\nabla^\perp P$$
$$-\frac{1}{A^*_{s,f}\rho_s}\left|\vec{S}\right|\nabla^\perp P_s + \frac{1}{A^*_{s,f}}\left(\alpha_s + \lambda_l\alpha_l\rho_l\frac{\beta_{ls} + \dot{m}_{ls}}{\rho_s}\right)_f \vec{g}\cdot\vec{S} \quad (36)$$

Replacing the face fluxes in (34) by (35) and (36), and collecting the terms that contain the pressure gradient on the left-hand side and all other terms on the right-hand side, results in

$$\nabla\cdot\left\{\left[\frac{\alpha_{l,f}}{A^*_{l,f}}\left(\alpha_l + \lambda_s\alpha_s\frac{\beta_{ls} + \dot{m}_{sl}}{\rho_s}\right)_f + \frac{\alpha_{s,f}}{A^*_{s,f}}\left(\frac{\alpha_s}{\rho_s} + \lambda_l\alpha_l\frac{\beta_{ls} + \dot{m}_{ls}}{\rho_s}\right)_f\right]\left|\vec{S}\right|\nabla^\perp P\right\}$$
$$= \nabla\cdot\left(\alpha_{l,f}\varphi^0_l + \alpha_{s,f}\varphi^0_s\right) \quad (37)$$

where φ^0_l and φ^0_s are the fluid- and solid-phase volumetric fluxes without the contribution of the pressure gradient, which are given by

$$\varphi^0_l = \frac{1}{A^*_{l,f}}[H_l + \lambda_s(\beta_{ls} + \dot{m}_{sl})H_s]_f\cdot\vec{S} - \frac{1}{A^*_{l,f}}\left(\lambda_s\frac{\beta_{ls} + \dot{m}_{sl}}{\rho_s}\right)_f \left|\vec{S}\right|\nabla^\perp P_s$$
$$+\frac{1}{A^*_{l,f}}[\alpha_l\rho_l + \lambda_s\alpha_s(\beta_{ls} + \dot{m}_{sl})]_f\vec{g}\cdot\vec{S} \quad (38)$$

$$\varphi^0_s = \frac{1}{A^*_{s,f}}\left(H_s + \lambda_l\frac{\beta_{ls} + \dot{m}_{ls}}{\rho_S}H_l\right)_f \cdot\vec{S} - \frac{1}{A^*_{s,f}\rho_s}\left|\vec{S}\right|\nabla^\perp P_s$$
$$+\frac{1}{A^*_{s,f}}\left(\alpha_s + \lambda_l\alpha_l\rho_l\frac{\beta_{ls} + \dot{m}_{ls}}{\rho_s}\right)_f \vec{g}\cdot\vec{S} \quad (39)$$

After solving the pressure equation and updating the pressure field, (40) and (41) are used to correct the flux of each phase using the new pressure field:

$$\varphi_l = \varphi^0_l - \frac{1}{A^*_{l,f}}\left(\alpha_l + \lambda_S\alpha_S\frac{\beta_{ls} + \dot{m}_{sl}}{\rho_s}\right)_f \left|\vec{S}\right|\nabla^\perp P \quad (40)$$

$$\varphi_s = \varphi^0_s - \frac{1}{A^*_{s,f}}\left(\frac{\alpha_s}{\rho_s} + \lambda_l\alpha_l\frac{\beta_{ls} + \dot{m}_{ls}}{\rho_s}\right)_f \left|\vec{S}\right|\nabla^\perp P \quad (41)$$

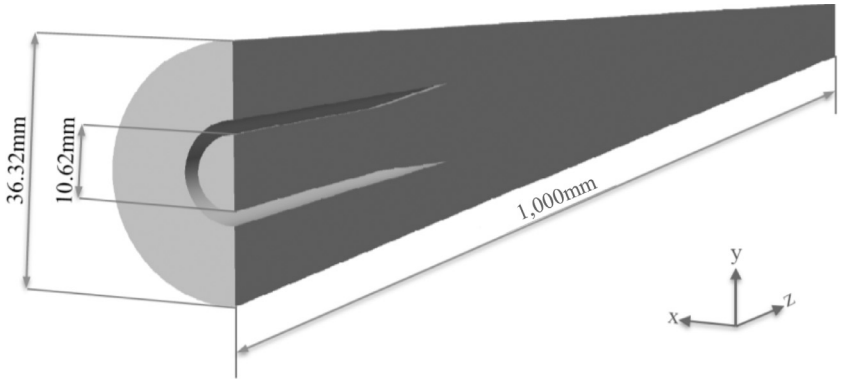

Fig. 2. Computational domain with inner tube diameters of 10.62 and 36.32 mm and length of 1 m (1000 mm). The two feeds are on the left and the outlet is on the right.

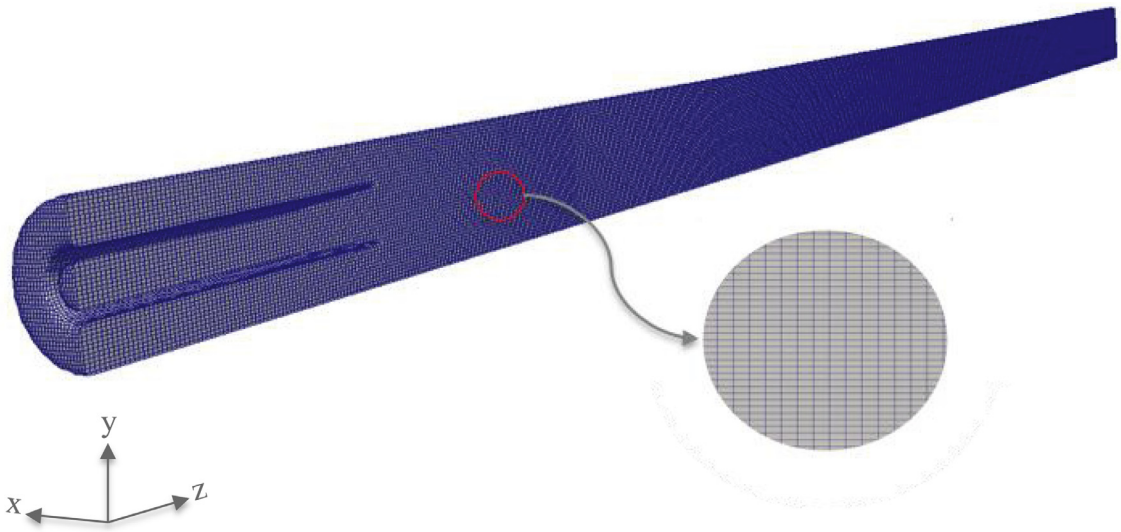

Fig. 3. Hex-dominant mesh used in the simulations.

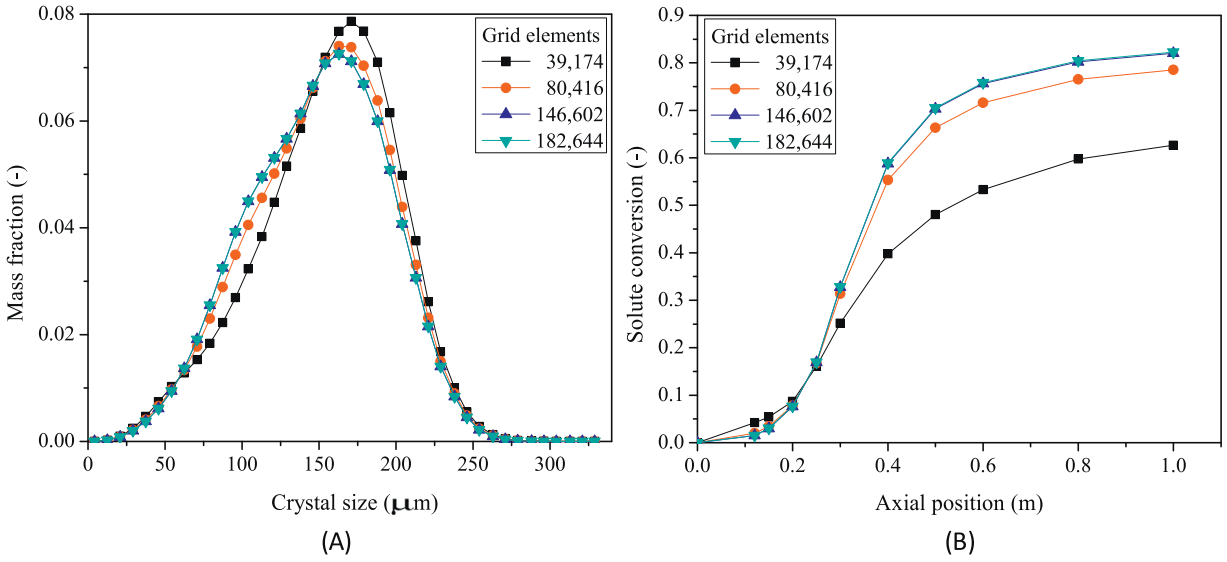

Fig. 4. Grid-independent numerical solution analysis: (A) average CSD at the outlet of the crystallizer; (B) solute conversion as function of the axial position.

3.3. Discretization of the crystals phase continuity equation

Discretizing the dispersed phase continuity equation requires special care, to ensure that the dispersed phase fraction is bounded between zero and the maximum physical value, which is the packing limit ($\alpha_{s,\,\max}$). The boundedness is achieved by re-formulating the continuity equation and implicitly introducing the solid pressure gradient into the continuity equation. By rewriting (2) for a constant density phase, using the face velocity flux to discretize the convective term, and introducing the mixture flux, $\varphi = \alpha_{l,f}\varphi_l + \alpha_{s,f}\varphi_s$ and the relative flux, $\varphi_r = \varphi_s - \varphi_l$, the continuity equation can be rewritten as

$$\frac{\partial \alpha_s}{\partial t} + \nabla \cdot \left(\alpha_{s,f}\varphi\right) + \nabla \cdot \left(\alpha_s \alpha_l \varphi_r\right) = \frac{\dot{m}_{ls} - \dot{m}_{sl}}{\rho_s} \tag{42}$$

Then the mixture and relative fluxes are replaced by the modified fluxes,

$$\varphi = \varphi^* - \alpha_{s,f}\frac{1}{A^*_{s,f}\rho_s}\left|\vec{S}\right|\nabla^{\perp}P_s \tag{43}$$

$$\varphi_r = \varphi_r^* - \frac{1}{A^*_{s,f}\rho_s}\left|\vec{S}\right|\nabla^{\perp}P_s \tag{44}$$

which explicitly include the solid pressure gradient, leading to the implemented form of the continuity equation as

$$\frac{\partial \alpha_s}{\partial t} + \nabla \cdot \left(\alpha_{s,f}\varphi^*\right) + \nabla \cdot \left(\alpha_s \alpha_l \varphi_r^*\right) - \nabla \cdot \left(\alpha_{s,f}\frac{1}{\boldsymbol{A}^*_{s,f}\rho_s}\left|\vec{S}\right|\nabla^{\perp}P_s\right) = \frac{\dot{m}_{ls} - \dot{m}_{sl}}{\rho_s} \tag{45}$$

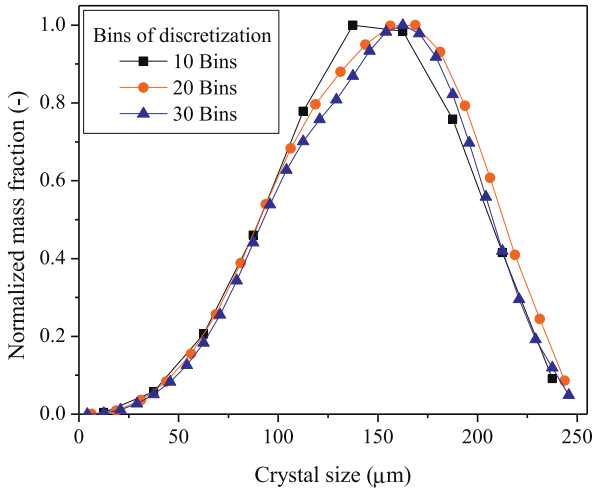

Fig. 5. Crystal mass distributions for varying numbers of bins used in the discretization of the internal coordinate.

3.4. Numerical solution procedure

The simulations were run using the merged PISO-SIMPLE (PIMPLE) algorithm, which combines the SIMPLE algorithm and the pressure implicit with splitting the operators (PISO) algorithm to rectify the second pressure correction and correct both velocities and pressure explicitly. The numerical solution procedure, adopted in the simulations, is summarized in Fig. 1.

As in Passalacqua and Fox (2011), the Euler implicit scheme was used to discretize the transient terms, the divergence of the phase stress tensor was discretized explicitly with the second-order central scheme, and the convective terms were discretized with a second-order upwind scheme with limited gradients. Transient simulations were run up to 20 s of real time simulation. A time step of 1.0×10^{-4} s was used in all simulations. A maximum residual of 1.0×10^{-3} was used for the momentum and turbulence model equations and 1.0×10^{-6} was used for all other equations.

4. Case study

4.1. Computational domain

The set of model equations was applied to simulate a coaxial crystallizer configuration of Pirkle et al. (2015). According to the authors coaxial crystallizers have negligible buildup of crystalline material on their surfaces and are less likely to plug.

A 3D computational domain with $YZ|_{x=0}$ plane of symmetry and an inner tube diameter of 0.01620 m and an outer tube diameter 0.03632 m, as shown in Fig. 2, was used in the simulations. The FreeCAD open-source CAD modeler was used to generate the geometry and export all the faces as STL(*StereoLithography*) files.

4.2. Mesh

3D computational meshes, with a $YZ|_{x=0}$ symmetry plane, were generated using the snappyHexMesh tool, available on OpenFOAM®. This tool generates hex-dominant meshes, as shown in Fig. 3, which contributes to numerical stability. A grid-independent numerical solution analysis was performed by keeping a constant time step throughout the simulations and varying the number of grid cells, as shown in Fig. 4A,B. The solute conversion as function of the axial coordinate and the CSD at the outlet of the crystallizer were chosen to compare the solutions because these variables strongly depend on all other parameters of the model. Increasing the number of grid cells from 39,174 up to 146,602 elements significantly affected the simulation results (Fig. 4A and B). However, further increments in the number of elements had no significant impact in the evaluated variables. Therefore, all the results shown in this article were run with a grid size of 146,602 elements.

4.3. Grid spacing for the PBE internal coordinate discretization

The number of bins to use for discretization of the internal coordinate (crystal growth axis), which fixes the Δr, was determined by comparing the mass-weighted average CSD at the outlet of the crystallizer for three different discretizations: 10 bins ($\Delta r =$ 25 μm), 20 bins ($\Delta r = 12.5$ μm), and 30 bins ($\Delta r = 8.33$ μm), which all correspond to a range of diameters between 0 and 250 μm (Fig. 5). Constant grid spacing was applied to discretize the crystal growth axis.

As it can be seen in Fig. 5, increasing the number of discretization bins from 10 to 20 significantly affected the CSD, shifting the maximum of the function to a larger crystal size. However, increasing from 20 to 30 bins produced results with an average crystal size of less than 0.5% difference. The differences between the outlet CSD for 20 and 30 bins in Fig. 4 are smaller than what would be detectable in experimental measurements, so no further increment in the number of bins was evaluated, and $\Delta r = 8.33$ μm was chosen to run all remaining simulations in this article. This discretization is in agreement with the grid spacing used in the simulation of antisolvent crystallization in dual impinging jet mixers of similar dimensions by Woo et al. (2009). The ability of the high-resolution finite volume method with a relatively small number of bins to provide good numerical accuracy in crystallizer simulations is consistent with past studies (Gunawan et al., 2004), in contrast to popular alternative numerical discretization methods such as the upwind difference and Lax–Wendroff methods that typically require 100 of bins to achieve similar numerical accuracy. In order to have a correct particle size distribution, it was necessary to run the sim-

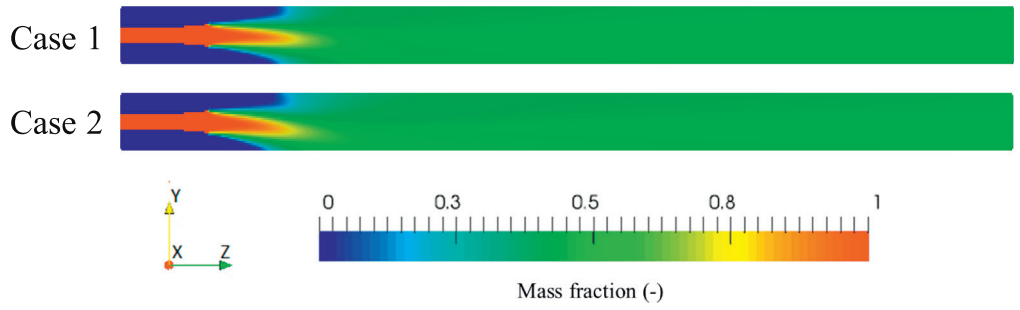

Fig. 6. Antisolvent mass fraction contour plot at the $YZ|_{x=0}$ plane of symmetry.

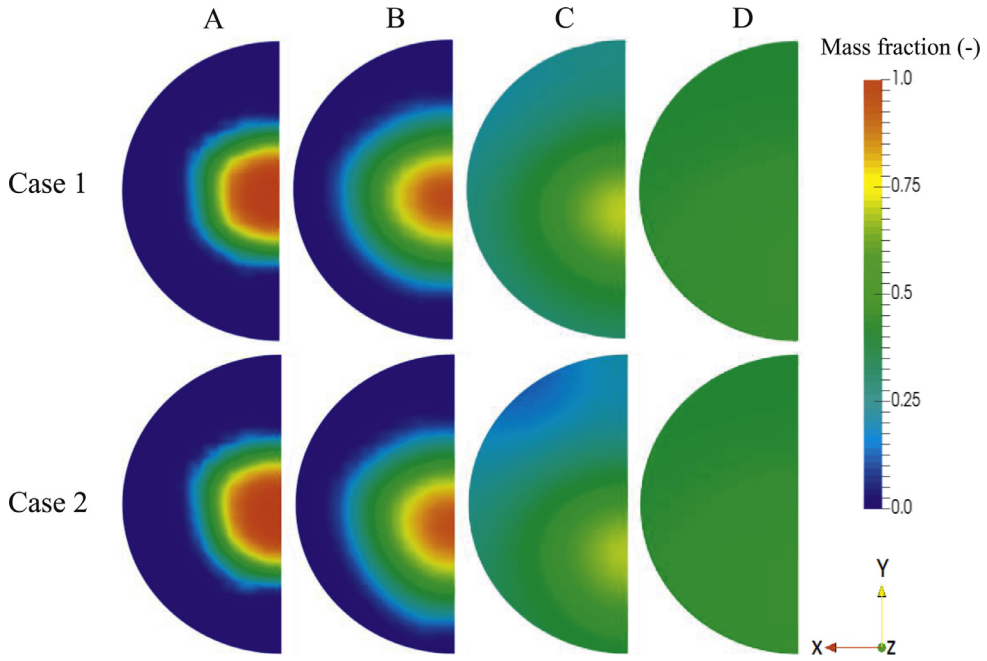

Fig. 7. Antisolvent mass fraction contour plot for XY planes at different axial positions: (A) 0.12 m; (B) 0.15 m; (C) 0.2 m; (D) 0.3 m.

Table 1
Operating conditions studied in this work.

	Component	Mass fraction		Mass flow rate (kg/s)	Inlet velocity (m/s)
		Outer tube inlet	Inner tube inlet		
Case 1	Solute	0.05	0	0.025	0.7876
	Solvent	0.95	0	0.475	
	Antisolvent	0	1	0.5	6
Case 2	Solute	0.05	0	0.0165	0.525
	Solvent	0.95	0	0.3135	
	Antisolvent	0	1	0.33	4

ulations with 40 bins of discretization, keeping the $\Delta r = 8.33$ μm, which correspond to a range of diameters between 0 and 333 μm.

4.4. Operating conditions

Simulations were performed for the solution of lovastatin/methanol (solute/solvent) fed through the outer tube inlet at a temperature of 305 K, and the antisolvent (pure water) fed through the inner tube inlet at a temperature of 293 K. The density of lovastatin is 1273 kg/m^3, and the volume shape factor was assumed to be 0.000625 (Pirkle et al., 2015). Two different total inlet mass flow rates were studied, 1.0 kg/s (Case 1) and 0.66 kg/s (Case 2), keeping the antisolvent/solution ratio equal to 1.0 in both cases, as shown in Table 1.

5. Results and discussion

Fig. 6 shows the contour plot of the antisolvent (water) mass fraction in the $YZ|_{x=0}$ plane of symmetry for the two cases. Asymmetric profiles in the Y coordinate are observed for both cases, which is due to the density difference between the antisolvent (heavier) and solution (lighter). The lower mass flow rate and inlet velocity in Case 2 than in Case 1 results in a stronger influence of gravity in the spatial profile even far down the crystallizer (Fig. 7C), which represents higher segregation of the antisolvent at the bottom of crystallizer and significantly affects the crystal nucleation and growth rates, as shown in Figs. 8 and 9, respectively. This result is interesting in that experimental studies on continuous crystallization in mixers typically do not consider the potential effects of gravity during the experimental design, the execution of the experiments, or in the interpretation of the experimental results (e.g., am Ende and Brenek, 2004; Jiang et al., 2015). The simulation shows that the effects of gravity on crystallization can be significant even for tubes that have diameters less than 4 cm.

The small increase in the inlet feed velocity (Case 1) provides better macro-mixing, which contributes to more spatially uniform profiles for crystal nucleation and growth rates (Figs. 8 and 9) and higher values of relative supersaturation, as shown in Fig. 10. The change in the peak relative supersaturation changes by more than 25%, which is important in practical applications as the amount of impurity incorporation into the crystals is typically a strong function of the relative supersaturation (e.g., Sangwal and Pałczyńska, 2000; Simone et al., 2015). The better macro-mixing and higher relative supersaturation values, which produced higher crystal nucleation and growth rates for Case 1 resulted, as expected, in higher solute conversion, for the same contact time, when compared to Case 2 (Fig. 11). That a higher initial momenta leads to enhanced mixing is not surprising; however, the relatively large mag-

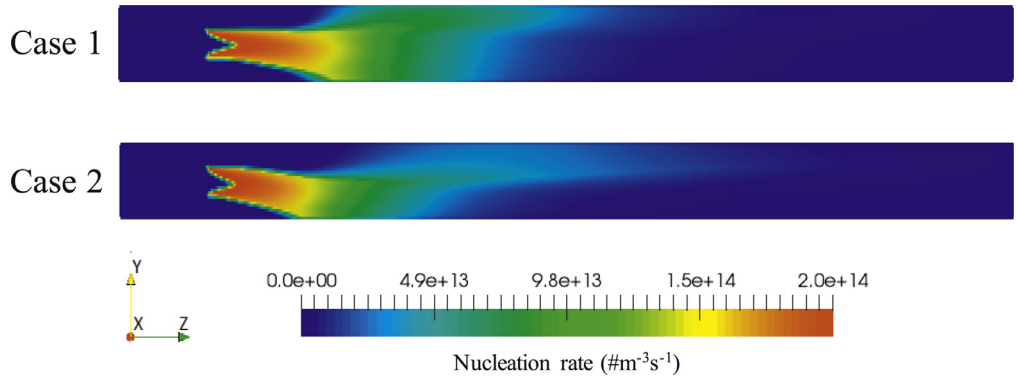

Fig. 8. Crystal nucleation rate contour plot at the $YZ|_{x=0}$ plane of symmetry.

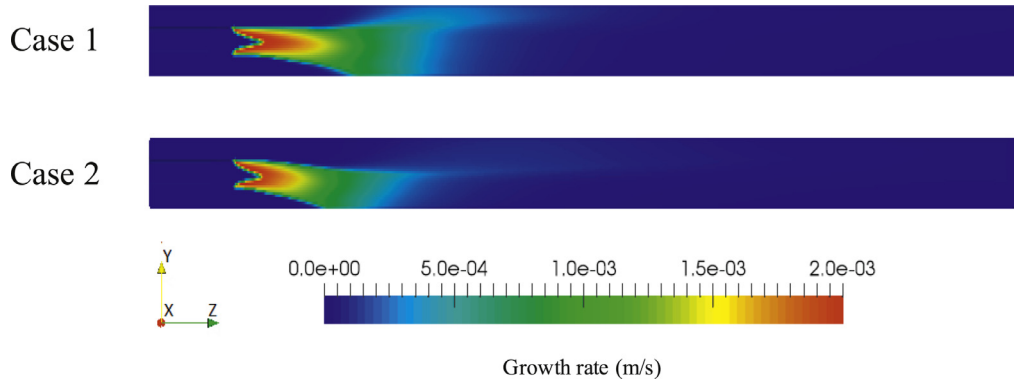

Fig. 9. Crystal growth rate contour plot at the $YZ|_{x=0}$ plane of symmetry.

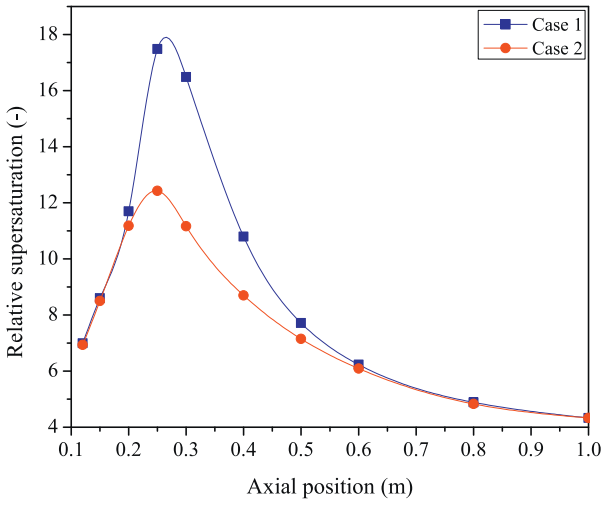

Fig. 10. Radially averaged relative supersaturation as function of the axial coordinate (the average is on a mass basis).

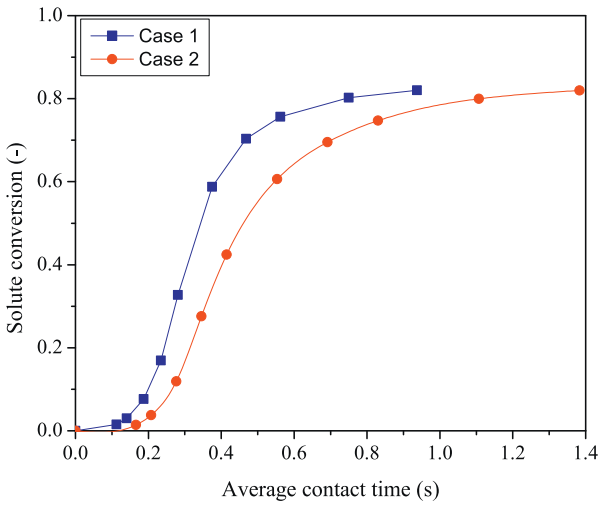

Fig. 11. Solute conversion as a function of the average contact time.

nitude of the change in the spatial evolution of the nucleation and growth rates and the relative supersaturation due to a relatively small increase in inlet feed velocity may be surprising to some.

Fig. 12 shows the cross-sectional profile of the crystals-phase volume fraction for different axial positions. It can be observed, as expected, that initially (Fig. 12A) the crystallization occurs at the interface between the solution and the antisolvent, where high supersaturation is generated. The asymmetric profiles observed in Fig. 12 are a result of both the density difference between the solution and antisolvent (Fig. 7), as discussed before, and the density difference between the liquid and crystals phases. More importantly, from Fig. 12A–D, the gradual collection of crystals at the bottom of the crystallizer can be observed, which induce fouling as the crystals are in direct contact with the wall under supersaturated conditions. These results show the importance of modeling the effects of particle settling, and demonstrate the model capability to predict fouling formation. Although the inlet feed velocities for the two cases are within a factor of two, the Case 2 simulations showed a much higher tendency for the collection of crystals on the lower wall, and a much higher potential for fouling, compared to Case 1. This behavior is a result of the balance between

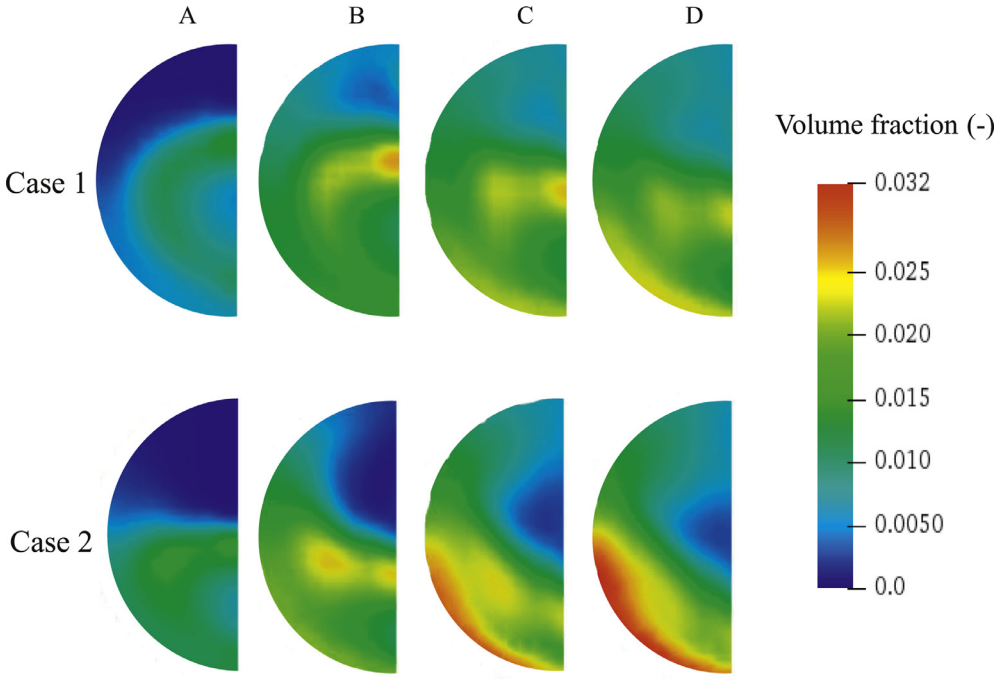

Fig. 12. Crystals-phase volume fraction contour plot for XY planes at different axial positions: (A) 0.3 m; (B) 0.5 m; (C) 0.8 m; (D) 1.0 m.

the momentum transfer, from the fluid to crystals phase, and the effect of gravity on both the solution and the crystals.

The use of a set of semi-discrete PBEs enables the model to predict the full CSD at every grid cell, which is one of the strengths of this formulation. Also, this approach enables the calculation of the flow properties of the crystals, using granular kinetic theory, based on the mean Sauter diameter of the full CSD at every grid cell. This ability is demonstrated in Fig. 13A and B for Cases 1 and 2.

The low crystals concentration and high supersaturation observed near the solution/antisolvent contact position (0.10 m) in continuous-flow antisolvent crystallization make nucleation the dominant phenomena for low contact time, which explains the narrower CSD and smaller average crystal size in Case 1 observed for the axial positions up to 0.20 m (Fig. 13AB). As the slurry moves downstream, the crystals concentration and mean crystal size increase with increasing contact time, the growth phenomena becomes dominant, and the mass fraction of fine crystals (e.g., < 10 μm) become negligible. The variation of the velocity as a function of the pipe radius also broadens the CSD, as liquid and crystals near the center move faster than liquid and crystals near the pipe walls. The Case 1 operating conditions produces narrower CSDs and smaller crystals at every axial position than for Case 2. For the kinetics model used here, as for nearly all solute-solvents systems, the dependency of the crystal nucleation rate on the relative supersaturation is stronger than for the growth rate. Since Case 1 presented better mixing and, consequently, higher values of the relative supersaturation in the first 40% of the crystallizer (Fig. 10), the ratio between the nucleation and growth rates is higher for Case 1, which generates more nuclei and, consequently, smaller crystals.

More interesting is that the shape of the outlet CSD is also qualitatively very different, with Case 2 producing a bimodal distribution whereas the distribution produced by Case 1 is nearly unimodal. Such bimodal distributions have not been observed in simpler simulation models that have been published for crystallization within such mixers (e.g., Pirkle et al., 2015), and one of the strengths of the formulation in this article is its ability to model all of the phenomena that contribute to the formation of such bimodal distributions. Also, bimodal distributions are difficult to discover and can result in large errors in formulations that employ some methods of moments in place of solving the population balance equations (e.g., see the computational results of Marchisio et al., 2002 and Falola et al., 2013).

6. Conclusions

A two-phase Eulerian-Eulerian model with variable properties coupled with granular kinetic theory, semi-discrete population balance equations, energy balance, and scalar transport equations was successfully implemented in the open-source CFD package OpenFOAM®. This model computes the spatial evolution of all crystallization states including the crystal size distribution, and is able to predict multimodal distributions as well as operating conditions that are prone to fouling, while taking into account the effects of turbulence and particle settling.

This model was applied to study the methanol/water antisolvent crystallization of Lovastatin in a coaxial crystallizer. As expected, the case study with higher inlet velocities (Case 1) showed better mixing, higher values of relative supersaturation, narrower CSD, and higher solute conversion when compared to Case 2. In addition, the crystals nucleation and growth rates are higher near the solution/antisolvent contact position, where high values of relative supersaturation are observed. The model also made many interesting predictions, which would not have been obvious without the capabilities provided by the model, including that (1) the spatial fields for the antisolvent mass fraction and crystal nucleation and growth rates can be highly asymmetric for small continuous-flow crystallizers ($<$4 cm in diameter) of symmetric configuration, (2) the effects of gravity on the liquid solution can be highly significant for small continuous-flow crystallizers, (3) a relatively small change in inlet feed velocity can generate a relatively large magnitude of the change in the spatial evolution of the nucleation and growth rates and the relative supersaturation, (4) continuous-flow crystallizers of small dimension can generate bimodal crystal size distributions for solute-solvents systems that are not experienced aggregation, agglomeration, or breakage, and (5) a relatively small

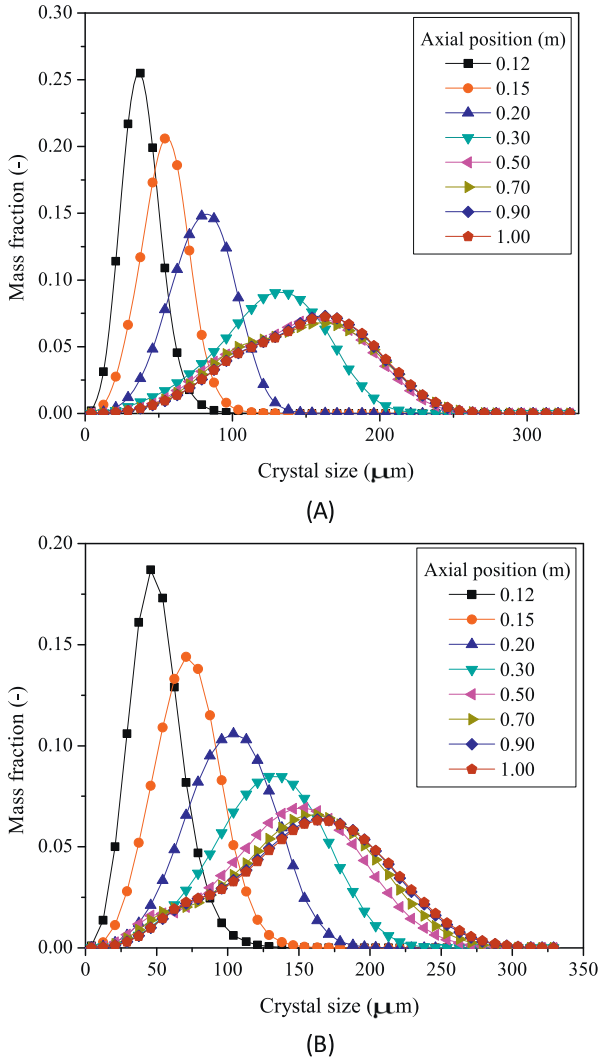

Fig. 13. Radially averaged crystal size distribution at different axial positions obtained for (A) Case 1 and (B) Case 2 (the average is on a mass basis).

change in the inlet feed velocity can change the crystal size distribution from being unimodal to bimodal. These results demonstrate the potential of the proposed mathematical formulation for gaining insights into continuous-flow crystallization that can be useful for the design of equipment or operations.

References

Abbasi, E., Abbasian, J., Arastoopour, H., 2015. CFD–PBE numerical simulation of CO_2 capture using MgO-based sorbent. Powder Tech 286, 616–628.

Ahmadzadeh, A., Arastoopour, H., Teymour, F., Strumendo, M., 2008. Population balance equations' application in rotating fluidized bed polymerization reactor. Chem. Eng. Res. Des. 86, 329–343.

Brahim, F., Augustin, W., Bohnet, M., 2003. Numerical simulations of the fouling process. Int. J. Therm. Sci. 42, 323–334.

Cheng, J.C., Yang, C., Jiang, M., Li, Q., Mao, Z.S., 2017. Simulation of antisolvent crystallization in impinging jets with coupled multiphase flow-micromixing-PBE. Chem. Eng. Sci. 171, 500–512.

am Ende, D., Brenek, S.J., 2004. Strategies to control particle size during crystallization processes. Am. Pharm. Rev. 7 (3), 98–104.

Falola, A., Borissova, A., Wang, X.Z., 2013. Extended method of moment for general population balance models including size dependent growth rate, aggregation and breakage kernels. Comput. Chem. Eng. 56, 1–11.

Gidaspow, D., 1994. Multiphase Flow and Fluidization. Academic Press, Inc, San Diego.

Gidaspow, D., Bezburuah, R., Ding, J., 1992. Hydrodynamics of circulating fluidized beds: Kinetic theory approach. In: Proceedings of the Seventh Engineering Foundation Conference on Fluidization, pp. 75–82.

Gunawan, R., Fusman, I., Braatz, R.D., 2004. High resolution algorithms for multidimensional population balance equations. AIChE J 50, 2738–2749.

Jasak, H., 1996. Ph.D. thesis. Imperial College of Science, Technology and Medicine, London.

Jiang, M., Li, Y.D., Tung, H., Braatz, R.D., 2015. Effect of jet velocity on crystal size distribution from antisolvent and cooling crystallizations in a dual impinging jet mixer. Chem. Eng. Process. 97, 242–247.

Koswara, A., Nagy, Z.K., 2017. ON-OFF feedback control of plug-flow crystallization: A case of quality-by-control in continuous manufacturing. IEEE Life Sci. Lett. 3, 1–4.

Kurganov, A., Tadmor, E., 2000. New high-resolution central schemes for nonlinear conservation laws and convection–diffusion equations. J. Comput. Phys. 160, 241–282.

Li, J., Trout, B.L., Myerson, A.S., 2015. Multistage continuous mixed-suspension, mixed-product removal (MSMPR) crystallization with solids recycle. Org. Process Res. Dev. 20, 510–516.

Liu, Y., Hinrichsen, O., 2014. CFD modeling of bubbling fluidized beds using OpenFOAM®: model validation and comparison of TVD differencing schemes. Comput. Chem. Eng. 69, 75–88.

Lun, C.K.K., Savage, S.B., Jeffrey, D.J., Chepurniy, N., 1984. Kinetic theories for granular flow: inelastic particles in Couette flow and slightly inelastic particles in a general flow field. J. Fluid Mech. 140 323–256.

Majumder, A., Nagy, Z.K., 2015. Dynamic Modeling of encrust formation and mitigation strategy in a continuous plug flow crystallizer. Cryst. Growth Des. 15, 1129–1140.

Mahajan, A.J., Kirwan, D.J., 1994. Nucleation and growth kinetics of biochemicals measured at high supersaturations. J. Cryst. Growth 144, 281–290.

Marchisio, D.L., Barresi, A.A., Baldi, G., Fox, R.O., 2002. Comparison between the classes method and the quadrature method of moments for multiphase systems. In: Proceedings of the 8th International Conference on Multiphase Flows in Industrial Plants, pp. 283–300.

Mullin, J.W.W., 2001. Crystallization, fourth edition. Elsevier Butterworth-Heineman, Oxford.

Nagy, Z.K., Fujiwara, M., Braatz, R.D., 2008. Modelling and control of combined cooling and antisolvent crystallization processes. J. Process Control 18, 856–864.

Ogawa, S., Umemura, A., Oshima, N., 1980. On the equation of fully fluidized granular materials. J. Appl. Math. Phys. 31, 483–493.

Pääkkönen, T.M., Ojaniemi, U., Pättikangas, T., Manninen, M., Muurinen, E., Keiski, R.L., 2016. CFD modelling of $CaCO_3$ crystallization fouling on heat transfer surfaces. Int. J. Heat Mass Transfer 97, 618–630.

Passalacqua, A., Fox, R.O., 2011. Implementation of an iterative solution procedure for multi-fluid gas–particle flow models on unstructured grids. Powder Tech 213, 174–187.

Pirkle, C., Foguth, L.C., Brenek, S.J., Girard, K., Braatz, R.D., 2015. Computational fluid dynamics modeling of mixing effects for crystallization in coaxial nozzles. Chem. Eng. Process. 97, 213–232.

Powell, K.A., Bartolini, G., Wittering, K.E., Saleemi, A.N., Wilson, C.C., Rielly, C.D., Nagy, Z.K., 2015. Toward continuous crystallization of urea-barbituric acid: a polymorphic co-crystal system. Cryst. Growth Des. 15, 4821–4836.

Randolph, A.D., Larson, M.A., 1988. Theory of Particulate Processes. Academic Press, Inc., New York.

Ranz, W.E., Marshall, W.R., 1952. Evaporation from drops. Chem. Eng. Prog. 48, 141–146.

da Rosa, C.A., Braatz, R.D., 2018. Multiscale modeling and simulation of macromixing, micromixing, and crystal size distribution in radial mixers/crystallizers. Ind. Eng. Chem. Res. 57 (15), 5433–5441.

Sangwal, K., Pałczyńska, T., 2000. On the supersaturation and impurity concentration dependence of segregation coefficient in crystals grown from solutions. J. Cryst. Growth 212, 522–531.

Schall, J.M., Mandur, J.S., Braatz, R.D., Myerson, A.S., 2018. Nucleation and growth kinetics for combined cooling and antisolvent crystallization in an MSMPR system: estimating solvent dependency. Cryst. Growth Des. 18, 1560–1570.

Simone, E., Steele, G., Nagy, Z.K., 2015. Tailoring crystal shape and polymorphism using combinations of solvents and a structurally related additive. CrystEngComm 17, 9370–9379.

Wang, T., Lu, H., Wang, J., Xiao, Y., Zhou, Y., Bao, Y., 2017. Recent progress of continuous crystallization. J. Ind. Eng. Chem. 54, 14–29. doi:10.1039/c5ce01878a.

Wen, C.Y., Yu, Y.H., 1966. Mechanics of fluidization. Chem. Eng. Prog. Symp. Series 62, 100–111.

edited by Wey, J.S., Karpinski, P.H., 2002. Batch Crystallization. In: Myerson., A.S. (Ed.), Handbook of Industrial Crystallization. Butterworth-Heinemann, Boston, pp. 231–248. edited by.

Woo, X.Y., Tan, R.B.H., Chow, P.S., Braatz, R.D., 2006. Simulation of mixing effects in antisolvent crystallization using a coupled CFD-PDF-PBE approach. Cryst. Growth Des. 6, 1291–1303.

Woo, X.Y., Tan, R.B.H., Braatz, R.D., 2009. Modeling and computational fluid dynamics-population balance equation-micromixing simulation of impinging jet crystallizers. Cryst. Growth Des. 9, 156–164.

Yu, Z., Yeoh, A., Chow, P.S., Tan, R.B.H., 2016. Particle size control in batch crystallization of pyrazinamide on different scales. Process Res. Dev. 20, 2100–2107.